Journal of Artificial Intelligence and Data Mining (JAIDM), x(x): xxx-xxx, xxxx

Shahrood University of Technology

Journal of Artificial Intelligence and Data Mining (JAIDM)
Journal homepage: http://jad.shahroodut.ac.ir

Research paper

Conditional Spatial Gustafson-Kessel Clustering Algorithm Based on Information Theory for Segmenting Brain MRI Images

Ali Fahmi Jafargholkhanloo[1*], Mousa Shamsi[2] and Mahdi Bashiri Bawil[2]

1. Department of Engineering Sciences, Faculty of Advanced Technologies, University of Mohaghegh Ardabili, Namin, Iran.
2. Department of Bioelectric, Faculty of Biomedical Engineering, Sahand University of Technology, Tabriz, Iran.

Article Info

Article History:
Received 20 August 2025
Revised 24 October 2025
Accepted 30 November 2025

DOI:10.22044/jadm.2025.16712.2798

Keywords:
Brain MRI Segmentation, Conditional Spatial Gustafson-Kessel, Image Segmentation, Information Theory.

**Corresponding author: a_fahmi@uma.ac.ir (A. F. Jafargholkhanloo)*

Abstract

Magnetic Resonance Imaging (MRI) often suffers from noise and Intensity Non-Uniformity (INU), making segmentation a challenging task. The Fuzzy C-Means (FCM) algorithm, a widely used clustering method for image segmentation, is highly sensitive to noise, and its convergence rate depends on data distribution. FCM employs the Euclidean distance metric, which fails to adapt to variations in data point distributions within compact and similarly shaped clusters. Additionally, this metric is not locally adaptive to different cluster shapes. This paper introduces a Conditional Spatial Gustafson-Kessel Clustering Algorithm based on Information Theory (CSGKIT) to address these challenges. First, information theory is incorporated to enhance the algorithm's robustness against noise and improve segmentation accuracy. Second, the Mahalanobis distance replaces the Euclidean distance to better accommodate cluster shapes during the clustering process. Finally, a conditional spatial approach uses a fuzzy-weighted membership matrix to incorporate local spatial interactions between neighboring pixels. The proposed CSGKIT algorithm is evaluated on two datasets: the BrainWeb simulated dataset and the Open Access Series of Imaging Studies (OASIS) dataset. Experimental results indicate that CSGKIT outperforms other FCM-based algorithms in segmentation accuracy across various tissue types.

1. Introduction

Various imaging techniques, such as X-rays, Positron Emission Tomography (PET), Computed Tomography (CT), and Magnetic Resonance Imaging (MRI), are widely employed in medical analysis. Among these, MRI stands out as a non-invasive, radiation-free method that provides excellent soft tissue contrast, making it particularly suitable for brain tissue differentiation [1]. The human brain consists of soft tissues such as White Matter (WM), Gray Matter (GM), and Cerebrospinal Fluid (CSF), making MRI ideal for brain tissue analysis [2]. Different MRI sequences produce distinct gray-level intensity patterns that provide complementary information about tissue characteristics [3]. Commonly used modalities include T1-Weighted, T2-Weighted, and Fluid-Attenuated Inversion Recovery (FLAIR). T_1-Weighted images highlight healthy tissues, T_2-Weighted images emphasize pathological areas, and FLAIR detects edema by suppressing water signals [4-6].

Segmentation is a primary challenge in medical image analysis, particularly for disease diagnosis [7]. MRI images often contain artifacts such as noise, Intensity Non-Uniformity (INU, also known as bias field, which is a smooth spatial variation of intensities caused by scanner or coil inhomogeneities), and partial volume effects, complicating segmentation. Brain-specific tasks, such as tumor detection, further increase complexity. Manual segmentation is common but time-consuming and susceptible to variability [8,

9]. Automated methods, including thresholding, clustering, contour-based techniques, and deep learning, have been developed to address these issues [8, 10, 11]. Thresholding methods [12, 13] struggle with noise and intensity variations [14], while contour-based methods [15, 16] are sensitive to parameter tuning and INU [17]. Deep learning provides robust results but requires large datasets, slow training, and complex models [10, 11]. Clustering, widely used for image segmentation, groups similar data points into distinct clusters. This study emphasizes clustering-based methods to address segmentation challenges in MRI images.

Li et al. [18] introduced the Multiplicative Intrinsic Component Optimization (MICO) method, which leverages an energy framework for simultaneous tissue segmentation and MRI bias field estimation. MICO employs orthogonal basis functions for bias field estimation and a level-set approach dependent on image gradients, but its computational complexity is high due to frequent reinitialization and sensitivity to noise from the lack of local spatial information [19]. Although popular, the fuzzy c-means (FCM) algorithm does not account for pixel correlations, prompting the development of Conditional Spatial FCM (CSFCM) [20]. However, its inability to handle uncertainties in MRI images limits the robustness of CSFCM. Elazab et al. [21] developed Adaptively Regularized Kernel-based FCM (ARKFCM), which improves handling of local variations but struggles with edge over-smoothing and non-spherical data distributions [22]. Qiao et al. [23] utilized Gaussian Mixture Models (GMM) and K-means for stroke lesion segmentation, but these methods are affected by INU and sensitivity to initialization. To address INU and noise, Parakash and Kumari [24] proposed the Spatial FCM and Expectation-Maximization with Bias Correction (SFCMEMBC). However, SFCMEMBC performs poorly under severe INU and noise conditions, and GMM methods rely on Gaussian assumptions and have slow convergence.

Meta-heuristic algorithms are widely used in medical image analysis. Singh et al. [25] presented Multi-Objective Particle Swarm Optimization (MOPSO) for MRI denoising and segmentation. Ghosh et al. [26] introduced the Chaotic Firefly Algorithm (CFA) to address the initialization sensitivity of FCM, but CFA's effectiveness depends on the choice of chaotic map. The FCM algorithm often suffers from local optimization issues, with convergence highly dependent on initial conditions. It can be formulated as: (i) a discrete optimization problem by initializing membership degrees for each search agent, or (ii) a continuous optimization problem by initializing cluster centers [27]. Verma et al. [28] applied Particle Swarm Optimization (FCMPSO), and Tongbram et al. [29] used the Whale Optimization Algorithm (FCMWOA) for continuous optimization. Conversely, Fahmi and Shamsi [27] employed Grey Wolf Optimization (FCMGWO) for discrete optimization, which outperformed continuous approaches in segmentation tasks. Despite their advantages, meta-heuristic algorithms are time-consuming, and many, such as PSO and Firefly Algorithm (FA), require precise parameter tuning to balance exploration and exploitation, affecting segmentation accuracy if misconfigured. Classical thresholding methods, such as Otsu and Kapur's, struggle with multiple thresholds. To improve this, Bandyopadhyay et al. [30] developed the Altruistic Harris Hawk Optimization (AHHO) algorithm, though it is computationally expensive and performs poorly on images with broad valleys or flat regions in the histogram, often neglecting spatial information.

A robust FCM algorithm was proposed by Kouhi et al. [31] for brain MRI segmentation, integrating spatial constraints and local membership matrix information. While effective, its double membership calculation per iteration increases computational complexity. Tavakoli et al. [32] enhanced FCM with dual estimation using both original and denoised images for improved segmentation. Kumar et al. [33] introduced a kernel-based FCM with spatial neighborhood information to handle noise and vagueness, though picture fuzzy systems often lack robustness against noise and outliers. Accurate white matter segmentation, crucial for estimating reduced white matter volume—a marker for neurological disorders—remains challenging. Vinurajkumar and Anandhavelu [34] improved FCM with a histogram-based membership matrix and Lagrange multiplier approach but faced sensitivity to initialization and difficulties with minor white matter discontinuities. Kumar et al. [35] developed BCIFCMSNI to address noise and bias field artifacts, while Solanki and Kumar [36] proposed PIFCMS. However, both rely on precise parameter tuning, limiting their practicality. Kumar et al. [37] introduced FBKPCS with two regularization terms, though it struggles with random noise and requires parameter tuning. Mohammadi et al. [38] combined FCM and a modified watershed algorithm for meningioma segmentation in contrast-enhanced T1-weighted MRI. Singh et al. [39] proposed the IFLICM algorithm to handle INU and noise, and Jafrasteh et al. [40] introduced ESFCM with weighted least squares and structural

similarity index-based polynomial bias field correction.

This study proposes a Conditional Spatial Gustafson-Kessel Clustering Algorithm based on Information Theory (CSGKIT) to address challenges in brain tissue segmentation in MRI images. The algorithm provides robust and accurate segmentation across diverse image conditions:

1. Elliptical Cluster Adaptability: Unlike FCM-based methods (e.g., ARKFCM, CSFCM, SFCMEM, and BCIFCMSNI) that assume hyper-spherical clusters and use Euclidean distance, CSGKIT adopts an elliptical geometry with the Mahalanobis distance metric. This enhances adaptability for compact and irregularly shaped clusters, such as those in the CSF region.
2. Noise and INU Robustness: CSGKIT effectively handles noise and INU through a novel objective function, ensuring improved segmentation under challenging conditions.
3. Integration of Spatial Context: Building on CSFCM [20], CSGKIT employs a conditional spatial strategy that incorporates local spatial information via a fuzzy weighted membership matrix, enhancing robustness to noise and improving accuracy.
4. Application of Information Theory: By leveraging information theory, CSGKIT further enhances accuracy and edge preservation under noise and INU conditions, with minimal parameter tuning required.

Experimental evaluations demonstrate that CSGKIT outperforms its counterparts discussed in the literature, delivering superior segmentation accuracy and robustness under diverse imaging conditions.

The rest of this article is organized as follows: Section 2 reviews related work on fuzzy clustering algorithms. Section 3 details the proposed methodology. Section 4 explores the experimental results, and Section 5 tries to make a conclusion along with potentials for future research.

2. Related Works

The FCM algorithm, introduced by Bezdek [41], incorporated a membership matrix u_{ij} into the *K*-means algorithm to elevate its performance. For a grayscale image I with N pixels indexed by i, let $p_i=(x_i,y_i)$ denote the spatial coordinates of the i-the pixel and $g_i=I(p_i)$ denote its gray-level (intensity) value $i=1,2,\ldots,N$. The set of cluster centers is $V=\{v_1,v_2,\ldots,v_C\}$ that v_j denotes the coordinate of the j-th cluster center in the feature space. A membership matrix U_{ij} is assigned to pixel i in the j-th cluster *(j=1, 2,..., c)*. The cost function in FCM is defined as follows:

$$J_{FCM}=\sum_{i=1}^{N}\sum_{j=1}^{c}U_{ij}^{q}\left(g_i-v_j\right)^2 \quad (1)$$

with the following constraint:

$$\sum_{j=1}^{c}U_{ij}=1\,\forall i \quad (2)$$

where v_j and q *(q>1)* are cluster center and fuzzy exponent, respectively.

In the FCM, the membership function and cluster centers will be updated iteratively as follows:

$$U_{ij}^{t+1}=\frac{1}{\sum_{j=1}^{c}\left(\frac{g_i-v_k^{t2}}{g_i-v_j^{t2}}\right)^{\frac{2}{q-1}}} \quad (3)$$

$$v_j^{t+1}=\frac{\sum_{i=1}^{N}\left(\left(U_{ij}^{q}\right)^{t}x_i\right)}{\sum_{i=1}^{N}\left(U_{ij}^{q}\right)^{t}} \quad (4)$$

Algorithm 1 summarizes the algorithmic steps for FCM.

Algorithm 1
Steps of FCM Clustering.

Input: MRI image, count of cluster centers, fuzzy exponent q, and stop criterion η
Step 1: Initializing membership matrix $U^{(t)}$
Step 2: Updating cluster centers $V^{(t+1)}$ using (4).
Step 3: Updating membership matrix $U^{(t+1)}$ using (3).
Step 4: if $\max U^{(t+1)}-U^{(t)}\leq\eta$, then proceed, otherwise set $t=t+1$ and return to **Step 2**
Output: cluster centers and membership matrix.

Szilágyi et al. [42] proposed the Enhanced FCM (EnFCM) algorithm, which exploits gray-level histograms to improve computational efficiency in MRI brain image segmentation. By a linear-weighted sum of local neighborhood information and the original image, EnFCM reduces computational time. To address its limitations, Cai et al. [43] incorporated a local similarity index to introduce the Fast Generalized FCM (FGFCM) algorithm, which improves noise robustness and detail preservation through a non-linear-weighted sum, while also achieving lower computational time. However, both EnFCM and FGFCM require parameter tuning to balance robustness and detail preservation. To overcome this, Krinidis and Chatzis [44] substituted parameters with a fuzzy local similarity index to develop the Fuzzy Local Information C-Means (FLICM) algorithm. Despite its improvements, FLICM's fixed spatial distance is less effective with varying local image information. Gong et al. [45] addressed this by introducing the Kernel-based Weighted Fuzzy Local Information C-Means (KWFLICM) algorithm, which handles intensity

inhomogeneities and noise, although its high computational complexity remains a limitation. Lei et al. [46] integrated morphological reconstruction and membership filtering to suggest the Fast and Robust FCM (FRFCM), which reduces computational time using gray-level histograms. However, FRFCM may produce overly smooth contours, compromising segmentation. Wang et al. [47] further attempted handling segmentation under unknown noise conditions by developing the Weighted ℓ_2-norm Regularization (WRFCM) algorithm from the Residual-Driven FCM (RFCM).

Traditional FCM assumes spherical clusters, which work well for uniformly sized and shaped clusters. However, the Gustafson-Kessel (GK) algorithm is more effective in identifying ellipsoidal clusters of varying sizes and orientations [48, 49]. It should be noted that the terms "spherical" and "ellipsoidal" clusters describe the geometry of clusters in the feature (parameter) space rather than the physical shape of regions in the image domain. By locally adapting the distance metric through covariance matrix estimation, the Mahalanobis distance—rather than the Euclidean distance—is used in the GK algorithm to identify clusters with distinct geometrical shapes [50, 51]. The GK algorithm's cost function is defined as follows:

$$J_{GK}=\sum_{i=1}^{N}\sum_{j=1}^{c}U_{ij}^{q}.\left(g_i-v_j\right)^{T}.A_j.\left(g_i-v_j\right) \tag{5}$$

where A_j is a positive definite symmetric norm matrix. By applying the Lagrange multiplier technique, the Equation 5 will be reformulated as an unconstrained optimization problem minimizing next cost function:

$$\begin{aligned}J_{GK}=&\sum_{i=1}^{N}\sum_{j=1}^{c}U_{ij}^{q}.\left(g_i-v_j\right)^{T}.A_j.\left(g_i-v_j\right)\\&-\sum_{i=1}^{N}\lambda_i\left(\sum_{j=1}^{c}U_{ij}-1\right)\\&+\sum_{j=1}^{c}\beta_j.\left(det\left(A_j\right)-\rho_j\right)\end{aligned} \tag{6}$$

where β_j a set of Lagrange multipliers. Also, ρ_j represents the cluster volume, typically considered to 1 for all clusters.

The membership function, cluster centers, and covariance matrix are updated as follows:

$$U_{ij}^{t+1}=\left(\frac{\left(g_i-v_r^{t}\right)^{T}.A_r^{t}.\left(g_i-v_r^{t}\right)}{\sum_{j=1}^{c}\left(g_i-v_j^{t}\right)^{T}.A_j^{t}.\left(g_i-v_j^{t}\right)}\right)^{1/q-1} \tag{7}$$

$$v_j^{t+1}=\frac{\sum_{i=1}^{N}\left(U_{ij}^{q}\right)^{t}.g_i}{\sum_{i=1}^{N}\left(U_{ij}^{q}\right)^{t}} \tag{8}$$

$$F_i^{t+1}=\frac{\sum_{i=1}^{N}\left(U_{ij}^{q}\right)^{t}.\left(g_i-v_j^{t}\right)^{T}.\left(g_i-v_j^{t}\right)}{\sum_{i=1}^{N}\left(U_{ij}^{q}\right)^{t}} \tag{9}$$

$$A_j^{t+1}=\lambda_i.\left(det\left(F_i^{t}\right)\right)^{\frac{1}{n}}.\left(F_i^{-1}\right)^{t} \tag{10}$$

where F_i models the weighted scatter of samples around the cluster center and reflects the geometric structure of the cluster.

The algorithmic steps for GK are summarized in Algorithm 2.

Algorithm 2
Steps of GK Clustering.

Input: MRI image, number of cluster centers, fuzzy exponent q, and stop criterion η.
Step 1: Initializing membership matrix $U^{(t)}$.
Step 2: Updating cluster centers $V^{(t+1)}$ using (8).
Step 3: Updating covariance matrix $F^{(t+1)}$ using (9).
Step 4: Updating norm matrix $A^{(t+1)}$ using (10).
Step 5: Updating membership matrix $U^{(t+1)}$ using (7).
Step 6: if $\max U^{(t+1)}-U^{(t)}\leq\eta$, then proceed, otherwise set $t=t+1$ and return to **Step 2**.
Output: cluster centers, covariance matrix, and membership matrix.

3. Proposed Algorithm

We propose the cost function of the CSGKIT algorithm for MRI image segmentation, defined as follows:

$$J_{CSGKIT}=\sum_{i=1}^{N}\sum_{j=1}^{c}\xi_i.U_{ij}^{q}.\left(g_i-v_j\right)^{T}.A_j.\left(g_i-v_j\right) \tag{11}$$

where ξ_i is an extra weighting coefficient designed to eliminate noisy samples. This coefficient represents the probability of image pixels and is determined by maximizing the mutual information between pixels value and cluster centers.

By applying the Lagrange multiplier technique, the Equation 11 will be transformed into an unconstrained optimization problem, minimizing the following cost function:

$$\begin{aligned}J_{CSGKIT}=&\sum_{i=1}^{N}\sum_{j=1}^{c}\xi_i.U_{ij}^{q}.\left(g_i-v_j\right)^{T}.A_j.\left(g_i-v_j\right)\\&-\sum_{i=1}^{N}\lambda_i\left(\sum_{j=1}^{c}U_{ij}-1\right)\\&+\sum_{j=1}^{c}\beta_j.\left(det\left(A_j\right)-\rho_j\right)\end{aligned} \tag{12}$$

where λ would be a Lagrange multiplier.

The derivative of J_{CSGKIT} with respect to u_{ij} and setting it equal to zero yields:

$$\frac{\partial J_{CSGKIT}}{\partial U_{ij}}=q.\xi_i.U_{ij}^{q-1}.\left(g_i-v_j\right)^{T}.A_j.\left(g_i-v_j\right)-\lambda_i=0 \tag{13}$$

Equation 13 is acquired by simplifying the relation and having λ. Equation 14 is utilized to update the membership matrix:

$$U_{ij}^{t+1}=\left(\frac{\left(g_i-v_r^t\right)^T.A_r^t.\left(g_i-v_r^t\right)}{\sum_{j=1}^{c}\left(g_i-v_j^t\right)^T.A_j^t.\left(g_i-v_j^t\right)}\right)^{1/q-1} \tag{14}$$

To obtain the cluster centers, the partial differential equation of J_{CSGKIT} with respect to v_j is computed and then set equal to zero:

$$\frac{\partial J_{CSGKIT}}{\partial v_j}=-2\sum_{i=1}^{N}\xi_i.U_{ij}^{\ q}.\left(g_i-v_j\right).A_j=0 \tag{15}$$

Equation 16 is utilized to update the cluster centers:

$$v_j^{t+1}=\frac{\sum_{i=1}^{N}\xi_i^t.\left(U_{ij}^{\ q}\right)^t.g_i}{\sum_{i=1}^{N}\xi_i^t.\left(U_{ij}^{\ q}\right)^t} \tag{16}$$

In the next step, the partial differential equation of J_{CSGKIT} with respect to A_j is computed and then set equal to zero:

$$\begin{aligned}\frac{\partial J_{CSGKIT}}{\partial A_j} &= \sum_{i=1}^{N}\xi_i.U_{ij}^{\ q}.\left(g_i-v_j\right)^T.\left(g_i-v_j\right)\\ &-\sum_{i=1}^{N}\left(\lambda_i.\frac{\partial}{\partial A_j}\left(det\left(A_j\right)\right)\right)\\ &=\sum_{i=1}^{N}\xi_i.U_{ij}^{\ q}.\left(g_i-v_j\right)^T.\left(g_i-v_j\right)\\ &-\sum_{i=1}^{N}\left(\lambda_i.U_{ij}^{\ q}.A_j^{-1}\right)=0\end{aligned} \tag{17}$$

By solving Equation 17, the corresponding solutions for A_j is obtained as follows:

$$F_i^{t+1}=\frac{\sum_{i=1}^{N}\xi_i^t.\left(U_{ij}^{\ q}\right)^t.\left(g_i-v_j^t\right)^T.\left(g_i-v_j^t\right)}{\sum_{i=1}^{N}\left(U_{ij}^{\ q}\right)^t} \tag{18}$$

$$A_j^{t+1}=\lambda_i\left(det\left(F_i^t\right)\right)^{\frac{1}{n}}.\left(F_i^{-1}\right)^t \tag{19}$$

In the final step, the mutual information between the input data $X=\{g_1,g_2,\ldots,g_N\}$ and the membership matrix distribution (U) is used to estimate ξ_i. Here, g_N represents the intensity of the j-th pixel in the MRI images. Mutual information based on information theory can be defined as follows [52]:

$$\begin{aligned}F\left(X,U\right) &= F\left(\mathrm{E}(X),\mathrm{E}(X|U)\right)\\ &=\sum_{i=1}^{N}\sum_{j=1}^{c}\mathrm{E}_i\mathrm{E}_{j|i}\log\left(\frac{\mathrm{E}_{j|i}}{\sum_{i=1}^{N}\mathrm{E}_i\mathrm{E}_{j|i}}\right)\end{aligned} \tag{20}$$

where ε_i is probability of i-th pixel and equal to ξ_i. Also, $\varepsilon_{j|i}$ is equal to u_{ij}. Therefore, Equation 20 can be modified as follows:

$$F(X,U)=\sum_{i=1}^{N}\sum_{j=1}^{c}\xi_i.U_{ij}.\log\left(\frac{U_{ij}}{\sum_{i=1}^{N}\xi_i.U_{ij}}\right) \tag{21}$$

By applying the Lagrange multiplier technique and considering $\sum_{i=1}^{N}\xi_i=1$ condition, Equation 21 can be reformulated as an unconstrained optimization problem, minimizing the next cost function:

$$J=\sum_{i=1}^{N}\sum_{j=1}^{c}\xi_i.U_{ij}.\log\left(\frac{U_{ij}}{\sum_{i=1}^{N}\xi_i.U_{ij}}\right)+\lambda\left(\sum_{i=1}^{N}\xi_i-1\right) \tag{22}$$

To obtain the ξ_i , the partial differential equation of J_{CSGKIT} with respect to ξ_i is computed and then set equal to zero:

$$-log(\xi_i)-1+\sum_{j=1}^{c}U_{ij}.log\left(U_{ij}\right)+\lambda=0 \tag{23}$$

Finally, according to Equation 23 and restricting condition, ξ_i can be updated as follows:

$$\xi_i^{t+1}=\frac{\exp\left(\sum_{j=1}^{c}U_{ij}^{\ t}.\log\left(\frac{U_{ij}^{\ t}}{\sum_{i=1}^{N}\xi_i.U_{ij}^{\ t}}\right)\right)}{\sum_{i=1}^{N}\exp\left(\sum_{j=1}^{c}U_{ij}^{\ t}.\log\left(\frac{U_{ij}^{\ t}}{\sum_{i=1}^{N}\xi_i.U_{ij}^{\ t}}\right)\right)} \tag{24}$$

Utilizing Equation 24 makes the proposed algorithm robust to noise. This process continues until the condition below is satisfied [52]:

$$\begin{cases}\xi_i^{t+1}=\dfrac{f_i^t}{\sum_{i=1}^{N}f_i^t}\\ f_i^t=\exp\left(\sum_{j=1}^{c}U_{ij}^{\ t}.\log\left(\dfrac{U_{ij}^{\ t}}{\sum_{i=1}^{N}\xi_i^t.U_{ij}^{\ t}}\right)\right)\\ \ln\left(\sum_{i=1}^{N}\xi_i^{t+1}.f_i^t\right)-\ln\left(\max\left(f_i^t\right)\right)<\delta\end{cases} \tag{25}$$

where δ is a small value that is equal to *1e-5*.

In MRI image processing, neighboring pixels are often highly correlated and depend on each other. The FCM algorithm performs inadequately without considering the correlation between neighboring pixels. Therefore, motivated by the concept of CSFCM [20], this study incorporates the local spatial relationships among neighboring pixels to employ a conditional spatial approach via a fuzzy weighted membership matrix. μ_{ij} is the first spatial conditional variable, which defines the degree of belonging of pixel g_k to the i-th cluster. This variable is used as follows:

$$\begin{cases}\mu_{ij}=\Psi_{ij}.U_{ij}\\ 0\le\Psi_{ij}\le1\end{cases} \tag{26}$$

where Ψ_{ij} represents the involvement level of pixel g_k in the i-th cluster and is computed by the following expression:

$$\Psi_{ij}=\frac{1}{M}\sum_{j\grave{o}N(x)}U_{ij} \tag{27}$$

where $N(x)$ is the square neighborhood with the pixel g at its center and M refers to the overall count of pixels in there. An expansive neighborhood may cause over-smoothing of edges and increase the misclassification rate of pixels [20]. In this study, to achieve the desired neighborhood level, we empirically set $N(x)=3\times3$.

The global membership U_{ij} and local membership μ_{ij} are assumed to be independent of each other. Two conditional variables, namely the weighted membership Z_{ij} and cluster center W_j are defined as follows by combining the global and local memberships:

$$Z_{ij} = \frac{\left(U_{ij}\right)^P . \left(\mu_{ij}\right)^L}{\Sigma_{j=1}^{C} \left(U_{ij}\right)^P . \left(\mu_{ij}\right)^L} \quad (28)$$

$$W_j = \frac{\Sigma_{i=1}^{N} \xi_i . {Z_{ij}}^q . g_i}{\Sigma_{i=1}^{N} \xi_i . {Z_{ij}}^q} \quad (29)$$

where L and P represent controller variables that define the relative significance of the membership functions. The mentioned variables establish a balance between global and local memberships to reconstruct the eventual membership values and cluster centers. Here, these parameters are set experimentally as $P=L=2$. For more detail about conditional spatial approach, refer to [20].

However, relying solely on Z_{ij} and W_j fails to attend the uncertainty degree that might exist in actual MRI images. This limitation may result in noisy pixels not being properly clustered within their neighborhood. To address this issue, the geometric mean of the global and local information is utilized, as follows:

$$U^{new}{}_{ij} = \sqrt{U_{ij} . Z_{ij}} \quad (30)$$

$$v^{new}{}_j = \sqrt{v_j . W_j} \quad (31)$$

The algorithmic steps for the presented CSGKIT are summarized in Algorithm 3.

Algorithm 3
Steps of Proposed CSGKIT Algorithm.

Input: MRI image, number of cluster centers, fuzzy exponent q, controller parameters (P, L), square neighborhood $N(x)=3$, initialization of cluster centers and input data distribution, and stop criterion η.
Step 1: Initializing membership matrix $U^{(t)}$.
Step 2: Updating covariance matrix $F^{(t+1)}$ using (18).
Step 3: Updating norm matrix $A^{(t+1)}$ using (19).
Step 4: Updating membership matrix $U^{(t+1)}$ using (14).
Step 5: Calculating ξ_i values using (25) until the condition of Equation 25 is met.
Step 6: Updating the conditional spatial membership using (26).
Step 7: Updating the weighted membership using (28).
Step 8: Updating joint cluster centers using (29).
Step 9: Updating cluster centers using (16).
Step 10: if $\max U^{(t+1)} - U^{(t)} \leq \eta$, then proceed, otherwise set $t=t+1$ and return to **Step 2**.
Output: new membership matrix (Equation 30), new cluster centers (Equation 31).

4. Experimental Results

We now present the experimental results and numerical analysis performed on grayscale MRI images. We also provide a comparative evaluation of the proposed algorithm against existing algorithms in the literature, including MICO [18], GMM [23], CSFCM [20], ARKFCM [21], FCMPSO [28], FCMWOA [29], FCMGWO [27], AHHO [30], SFCMEMBC [24], BCIFCMSNI [35], FRFCM [46], RFCM [47], and FBKPCS [37]. Both visual and quantitative comparisons are included. The experiments were conducted on an ACER desktop equipped with 16 GB of RAM and an Intel Core i7 CPU (2.60 GHz). To quantitatively evaluate the performance of the methods, we used three main criteria: Jaccard Similarity (*JS*), Dice Similarity (*DS*), and Correctly Matched Segments (*CMS*) [53].

Jaccard Similarity Coefficient (JS): The similarity between two images can be quantified by this metric, which is defined as:

$$JS(A,B) = \frac{|A \cap B|}{|A \cup B|} \quad (32)$$

Dice Similarity Coefficient (DS): The overlap between two images, specifically the ground truth (GT) and the segmented image, can be quantified by this metric, which is defined as:

$$DS(A,B) = \frac{2|A \cap B|}{|A| + |B|} \quad (33)$$

Contour Matching Score (CS): The contour alignment between the ground truth and the segmented image can be evaluated by this metric. The *CS* index ranges from 0 to 1, where a score of 1 indicates an impeccable match of object contours in the ground truth and the predicted image. This index is defined as:

$$CS = \frac{2.P^C . R^C}{P^C + R^C} \quad (34)$$

where R^C and P^C represent recall and precision, respectively. High *DS*, *JS*, and *CS* indicate a good performance of a clustering method with accurate segmentation and contour alignment.

4.1. Data Description

To evaluate the proposed CSGKIT algorithm against other methods, we conducted experiments on two brain MRI datasets: the BrainWeb simulated dataset [54] and the Open Access Series of Imaging Studies (OASIS) dataset [55]. The BrainWeb dataset includes simulated brain MRI images with varying INU levels (20%, 40%) and noise levels (3%, 9%). The images have a resolution of 1 mm and dimensions of 181 × 217 × 181, with ground truth available for different brain tissues. Segmentation was performed on T1-weighted images, focusing on slices 80 to 120. The OASIS dataset comprises a cross-sectional collection of 416 subjects aged 18 to 96 years, including 100 individuals clinically diagnosed with very mild to moderate Alzheimer's disease. For

this study, 200 T1-weighted MRI images were randomly selected, with skull stripping applied via morphological operations prior to segmentation.

4.2. Parameter Setting

In the numerical implementation of our proposed algorithm and the compared algorithms, several constant parameters need to be configured. For this study, three key parameters were defined: the fuzzy exponent *(q)*, the minimum error threshold *(η)*, and the maximum iterations. These parameters were set to $q=2$, $\eta = 10^{-5}$, and a maximum of 50 iterations for both all algorithms. In this study, the number of cluster centers C is set to 4, corresponding to the main brain tissue types including white matter (WM), gray matter (GM), cerebrospinal fluid (CSF) and the background. This selection ensures that each tissue class is captured by a distinct cluster, facilitating accurate and interpretable segmentation of MRI brain images. In the proposed algorithm, the local neighborhood is empirically defined as a 3×3 window centered at each pixel. This neighborhood size is chosen to effectively capture local spatial correlations among neighboring pixels, which is essential for preserving fine tissue boundaries while mitigating the influence of isolated noisy pixels. Through additional experiments with larger neighborhoods (e.g., 5×5 and 7×7), the results illustrated that while larger windows further smooth the membership maps, they may inadvertently blur edges and reduce sensitivity to subtle structural variations in the MRI data. Conversely, smaller neighborhoods may fail to capture sufficient local context, leading to increased susceptibility to noise. Therefore, the 3×3 region provides an optimal compromise, ensuring that local spatial information enhances the clustering process without sacrificing boundary definition or tissue differentiation. This choice is aligned with prior studies demonstrating that moderate neighborhood sizes in conditional spatial clustering yield robust segmentation results for brain MRI images. Also, the parameters P and L control the relative weighting of global and local memberships in the conditional spatial approach. In our experiments, different combinations (P,L)=(1,2),(2,1),(2,2) were tested. The combination (2,2) was found to yield the most effective segmentation results and was therefore adopted. In the MICO algorithm, the degree of Legendre polynomials was opted for $P=3$. For the CSFCM algorithm, controller parameters were set to $p=q=2$. For FCMPSO, as reported in [28], the population size *(n)*, cognitive coefficient, social coefficient, and inertia weight are set as $n=60$, $c_1=c_1=2$, and $\omega=1$, respectively. For FCMWOA and FCMGWO, the population size was $n=12$. For ARKFCM, no additional parameters beyond the fuzzy exponent, error threshold, and number of clusters were required. In the AHHO algorithm, parameters were configured as per the reported values, except for the number of thresholds. In BCIFCMSNI, Sugeno's negation parameter was set to $\beta = 1.7$, the spatial regularization parameter to $\alpha = 1.5$, and the neighborhood size to 3×3. For FRFCM, the structure element (*SE*) used for morphological reconstruction (MR) was defined as a square of size 3×3. In RFCM, the decreasing rate of the weighting matrix was controlled by the parameter, which was set to $\xi = 0.0008$. The β parameter in RFCM was configured based on the standard deviation of the image data, reflecting its association with noise levels. Lastly, for FBKPCS, two key parameters were defined: the bound and the spatial parameter, which were set to $C = 0.5$ and $\alpha = 0.3$, respectively.

4.3. Experimental Results on Brain Web Dataset

The segmentation performance was evaluated on simulated T1-weighted brain MRI images with INU levels of 20% and 40%, and noise levels of 3% and 9%, focusing on slices 80–120. Figure 1 shows qualitative segmentation results on an axial slice (slice 86) corrupted with 40% INU and 9% noise. Quantitative performance was assessed using *DS*, *JS*, and *CS* metrics, with average results for WM, GM, and CSF presented in Tables 1–3. Figure 2 plots the average *DS* values for brain tissues across slices 80–120 with 9% noise and 40% INU. Key insights from these results are discussed below:

(1) According to Table 1, the proposed algorithm produces better results than other methods in WM segmentation. Based on the *CS* criterion, the MICO algorithm struggles to accurately identify WM boundaries under high noise (9%) and INU levels (20% and 40%), although it performs well under lower noise (3%) conditions. Figure 2 highlights MICO's difficulties, particularly for slices 104–113. GMM, sensitive to noise and outliers due to its normal distribution assumption, also fails to segment WM effectively under these conditions, as shown in Table 1. The CSFCM demonstrates the best *DS* and *JS* values for WM segmentation at 9% noise and 20% INU, maintaining consistency across slices but underperforming with compact clusters like CSF. While ARKFCM achieves good WM segmentation, Figure 2 reveals limitations for slices 99–104. FCMPSO is less effective under high noise and INU, often mislabeling background pixels as GM, and struggles with slices 90–109. Conversely, FCMWOA performs better across

these slices, requiring fewer parameter adjustments, emphasizing PSO's limitations for FCM optimization. Discrete optimization in FCMGWO surpasses the continuous optimization of FCMPSO and FCMWOA, yielding more stable results (Figure 2). Additionally, as shown in Figure 1(g–i), FCMGWO resolves misclassification issues seen in FCMPSO and FCMWOA. The AHHO delivers comparable performance to FCMGWO but is more time-consuming and noise-sensitive due to its thresholding approach. SFCMEMBC performs well for WM segmentation but is less effective for GM and CSF, showing consistent results across slices (Fig. 2). BCIFCMSNI struggles with bias field corrections, particularly for slices 109–120, as evidenced by its low *JS* values in Table 1. Under varying noise (3%, 9%) and INU (20%, 40%) conditions, FRFCM, RFCM, and CSGKIT show robust WM segmentation. CSGKIT's reliance on information theory rather than MR enhances its robustness over FRFCM and RFCM. Table 1 indicates that CSGKIT achieves excellent edge preservation and contour matching, while Figure 2 confirms consistent performance across slices. Although FBKPCS is robust under varying conditions, its primary drawback lies in the manual tuning required for spatial and bounded parameters.

(2) As detailed in Table 2, the CSGKIT algorithm excels over other methods in GM segmentation under various noise and INU levels, particularly based on the *CS* criterion. CSGKIT demonstrates robust edge preservation and accuracy, achieving an average *CS* value of 98% under 9% noise and 20% INU, the highest among all methods, and performs best under 9% noise and 40% INU. The MICO algorithm performs poorly for GM segmentation based on *DS* and *JS* criteria due to its sensitivity to noise and INU. However, it achieves satisfactory results under low noise (3%) based on the *CS* criterion, effectively identifying GM boundaries. MICO struggles under high noise (9%), failing to segment GM accurately, unlike the consistently robust CSGKIT. FCMPSO exhibits the poorest performance across all conditions, frequently mislabeling background pixels as GM. While FCMWOA improves under low noise, it lacks robustness under higher noise and INU levels. Figure 2 shows BCIFCMSNI performs well for slices 80–85 and 92–102 but fails elsewhere, making it unreliable for GM segmentation. Three algorithms—CSFCM, FBKPCS, and CSGKIT—deliver reliable GM segmentation. However, CSFCM's spherical distance criterion limits its effectiveness for compact clusters. In contrast, CSGKIT achieves the highest *DS* values and excels in segmenting GM with detailed precision, as shown in Figure 2. Unlike GMM and SFCMEMBC, which fail due to normal distribution assumptions, CSGKIT preserves edges and captures fine details, outperforming its peers.

(3) CSF regions, composed of compact and small clusters, pose challenges for FCM-based approaches due to their reliance on Euclidean distance. Figure 1(m) shows that FRFCM mislabels CSF regions as GM, and Table 3 confirms that FCM-based methods struggle with CSF segmentation, especially when clusters vary in size and shape. This underscores their inadequacy for datasets with ellipsoidal clusters. The MICO algorithm performs better with compact clusters, as reflected in Table 3, but its performance is surpassed by CSGKIT. Among FCM-based methods, SFCMEMBC performs the poorest, frequently mislabeling CSF pixels as GM (Figure 1(k)). CSGKIT consistently achieves the highest scores across evaluation criteria, delivering stable performance under varying noise and INU levels. Its ability to detect ellipsoidal clusters of diverse sizes and orientations ensures robust and accurate CSF segmentation.

(4) The Table 4 highlights differences in computational efficiency among the algorithms. Iterative optimization methods like FCMPSO, are computationally expensive. Contour-based algorithms, also have longer execution times due to the dependency of their edge-stopping functions on the image gradient, increasing overhead. In contrast, FRFCM and CSGKIT demonstrate the shortest execution times. However, both face limitations when cluster sizes and shapes vary significantly. Despite this, FBKPCS and CSGKIT deliver robust segmentation performance on images with noise and INU, achieving these results with minimal elapsed time.

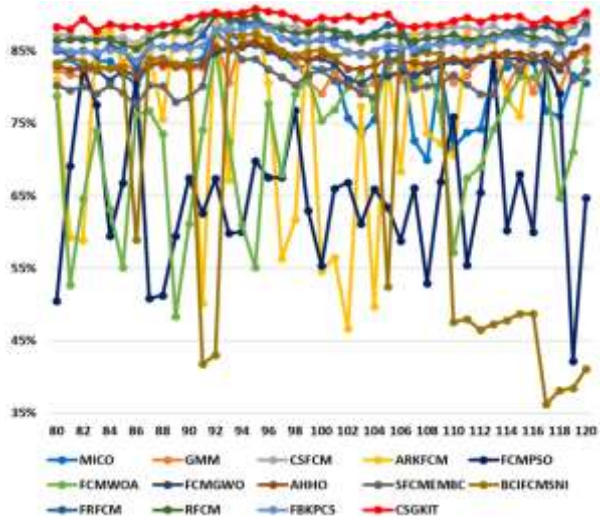

Figure 2. Performance of all assessed algorithms, including our proposed CSGKIT algorithm, in terms of the average *DS* criterion for WM, GM, and CSF across slices 80-120 of the Brain Web MRI dataset with 9% noise and 40% INU.

Table 1. Numerical results of all assessed algorithms, including our proposed CSGKIT algorithm, for WM segmentation on the Brain Web simulated dataset.

Criteria / Methods	*DS* (%) ↑				*JS* (%) ↑				*CS* (%) ↑			
	3% Noise		9% Noise		3% Noise		9% Noise		3% Noise		9% Noise	
	20% INU (μ±S.D)	40% INU (μ±S.D)	20% INU (μ±S.D)	40% INU (μ±S.D)	20% INU (μ±S.D)	40% INU (μ±S.D)	20% INU (μ±S.D)	40% INU (μ±S.D)	20% INU (μ±S.D)	40% INU (μ±S.D)	20% INU (μ±S.D)	40% INU (μ±S.D)
MICO	93.30±0.45	94.24±1.45	84.06±0.56	84.55±5.06	87.86±0.67	89.61±1.37	72.76±0.67	73.50±6.24	95.20±0.76	97.15±0.93	77.34±0.39	78.26±3.99
GMM	95.68±0.36	91.94±0.16	85.43±2.70	84.59±2.66	91.75±0.36	85.13±0.26	74.70±3.74	73.39±3.99	98.38±0.38	91.03±0.26	78.44±1.72	78.20±3.14
CSFCM	95.76±0.26	93.91±0.15	**94.25±1.24**	91.16±1.36	91.91±0.48	88.55±0.25	**89.16±2.19**	85.49±2.41	98.57±0.29	95.96±0.15	97.89±1.07	93.59±2.06
ARKFCM	94.96±3.59	92.91±4.47	93.11±3.01	90.63±31.58	91.90±4.37	86.88±4.21	87.19±2.99	82.97±30.73	98.57±2.52	93.55±1.76	94.27±0.64	89.80±7.50
FCMPSO	79.62±2.34	84.80±1.64	62.97±1.94	71.14±16.25	72.48±2.57	77.81±1.89	51.15±1.78	59.54±13.16	90.96±2.36	91.34±2.44	73.11±0.72	75.79±7.80
FCMWOA	91.76±3.67	88.65±3.79	80.35±3.05	82.20±15.06	85.51±3.34	81.55±3.35	69.31±2.98	70.88±14.18	92.52±3.22	87.27±3.36	76.92±3.24	77.76±10.05
FCMGWO	95.63±0.26	94.09±0.65	88.05±1.66	87.34±1.83	92.02±0.41	89.55±0.37	78.69±2.62	77.57±2.85	98.60±0.25	97.21±0.64	82.85±3.95	82.84±3.67
AHHO	95.12±0.26	93.70±0.49	88.21±1.78	87.60±1.96	92.28±0.38	89.98±0.46	78.94±2.82	77.98±3.06	99.04±0.24	96.41±0.37	83.34±3.49	83.53±3.25
SFCMEMBC	95.72±0.18	94.44±1.54	93.91±1.52	91.31±1.62	91.85±0.31	89.50±2.72	88.55±2.67	85.76±2.68	98.63±0.17	96.80±1.59	**98.08±1.39**	93.87±1.86
BCIFCMSNI	88.89±2.48	84.87±1.93	85.76±2.83	85.25±10.14	81.91±1.63	76.08±1.52	75.44±3.01	74.97±2.24	80.09±1.76	69.95±2.17	82.13±2.47	78.66±8.5
FRFCM	94.17±0.32	94.26±0.37	93.52±2.10	91.59±2.48	91.75±0.39	89.18±0.44	87.88±3.03	85.19±3.06	97.93±0.34	95.48±0.37	96.66±2.91	93.25±2.78
RFCM	94.36±0.22	93.19±0.41	93.79±2.43	91.17±2.45	90.63±0.36	87.29±0.34	88.84±3.21	85.83±3.18	97.26±0.27	94.14±0.21	97.05±2.88	93.41±2.98
FBKPCS	96.03±0.26	94.47±1.45	90.64±1.82	89.53±1.82	91.60±0.39	89.91±2.36	82.92±2.87	81.09±2.93	99.08±0.25	97.32±1.53	88.66±2.62	87.70±2.57
CSGKIT	**96.37±0.68**	**94.64±1.03**	92.82±1.43	**91.87±1.42**	**92.83±0.64**	**90.50±1.04**	86.65±2.33	**86.00±2.46**	**99.20±0.62**	**97.37±0.78**	94.17±1.42	**93.89±1.84**

Table 2. Numerical results of all assessed algorithms, including our proposed CSGKIT algorithm, for GM segmentation on the Brain Web simulated dataset.

Criteria / Methods	*DS* (%) ↑				*JS* (%) ↑				*CS* (%) ↑			
	3% Noise		9% Noise		3% Noise		9% Noise		3% Noise		9% Noise	
	20% INU (μ±S.D)	40% INU (μ±S.D)	20% INU (μ±S.D)	40% INU (μ±S.D)	20% INU (μ±S.D)	40% INU (μ±S.D)	20% INU (μ±S.D)	40% INU (μ±S.D)	20% INU (μ±S.D)	40% INU (μ±S.D)	20% INU (μ±S.D)	40% INU (μ±S.D)
MICO	87.52±0.43	89.10±0.74	75.04±0.43	75.69±3.65	78.30±0.68	80.61±0.70	60.33±0.47	61.20±3.96	97.60±0.31	97.36±0.57	91.90±0.41	92.20±4.16
GMM	91.80±0.34	87.44±0.23	80.02±2.61	79.13±2.51	84.88±0.35	77.76±0.37	66.78±3.13	65.54±3.46	98.73±0.28	94.48±0.23	91.84±2.09	91.33±2.60
CSFCM	90.19±0.24	88.48±0.18	**89.32±1.08**	86.56±1.17	82.20±0.38	79.39±0.29	**80.72±1.75**	76.60±1.78	96.76±0.15	95.85±0.16	97.60±1.15	95.45±1.41
ARKFCM	84.38±3.52	78.00±3.38	77.57±1.75	74.35±23.20	75.05±3.38	66.57±3.23	65.63±1.73	61.22±21.17	97.00±1.21	95.19±1.23	95.69±0.56	94.21±7.93
FCMPSO	67.34±3.01	67.86±3.23	59.15±2.09	58.82±12.87	52.28±2.87	57.22±2.98	45.45±1.73	44.66±12.43	92.63±1.22	91.64±1.29	88.40±0.82	88.22±6.78
FCMWOA	78.84±2.60	76.73±2.55	67.94±3.69	68.44±9.70	68.44±2.46	65.35±2.35	53.36±3.41	53.65±10.76	95.67±1.15	93.54±1.08	91.58±3.52	91.77±7.62
FCMGWO	91.39±0.36	90.10±0.48	81.03±1.39	80.33±1.56	83.37±0.47	82.17±0.45	68.13±1.96	67.15±2.18	98.62±0.28	98.10±0.35	94.16±1.30	93.80±1.37
AHHO	91.77±0.31	90.44±0.47	81.37±1.26	80.81±1.41	85.02±0.45	82.49±0.49	68.60±1.78	67.82±1.98	98.58±0.19	98.21±0.52	94.41±1.16	94.15±1.31
SFCMEMBC	84.40±0.25	83.41±2.30	83.92±2.65	82.78±2.17	73.09±0.38	71.61±3.43	72.37±3.42	70.68±3.18	92.33±0.20	91.41±1.97	93.99±1.86	92.89±1.78
BCIFCMSNI	68.95±2.71	66.74±2.61	69.81±2.53	67.96±3.25	61.00±1.72	58.92±1.64	55.58±1.21	55.00±1.05	89.79±1.89	84.78±1.37	93.94±2.51	91.18±4.13
FRFCM	89.51±0.48	88.22±0.56	86.81±1.16	85.21±1.98	81.09±0.61	78.98±0.32	76.74±0.91	74.12±2.53	94.86±0.19	93.75±0.21	94.70±0.46	93.11±2.25
RFCM	89.27±0.52	87.13±0.41	88.25±1.24	86.01±2.54	80.66±0.54	77.21±0.45	78.80±0.90	75.22±2.22	95.04±0.13	94.08±0.13	95.41±0.34	94.19±2.14
FBKPCS	91.58±0.32	90.27±1.72	84.66±1.16	83.48±1.26	84.72±0.47	82.20±2.49	73.41±1.78	71.66±1.87	98.52±0.21	98.24±1.02	96.20±0.95	95.44±1.16
CSGKIT	**92.81±0.69**	**90.70±0.85**	87.89±1.03	**86.68±1.04**	**86.62±1.01**	**83.10±1.29**	78.41±1.74	**76.93±1.78**	**99.34±0.51**	**98.42±0.81**	**97.69±0.76**	**96.77±1.17**

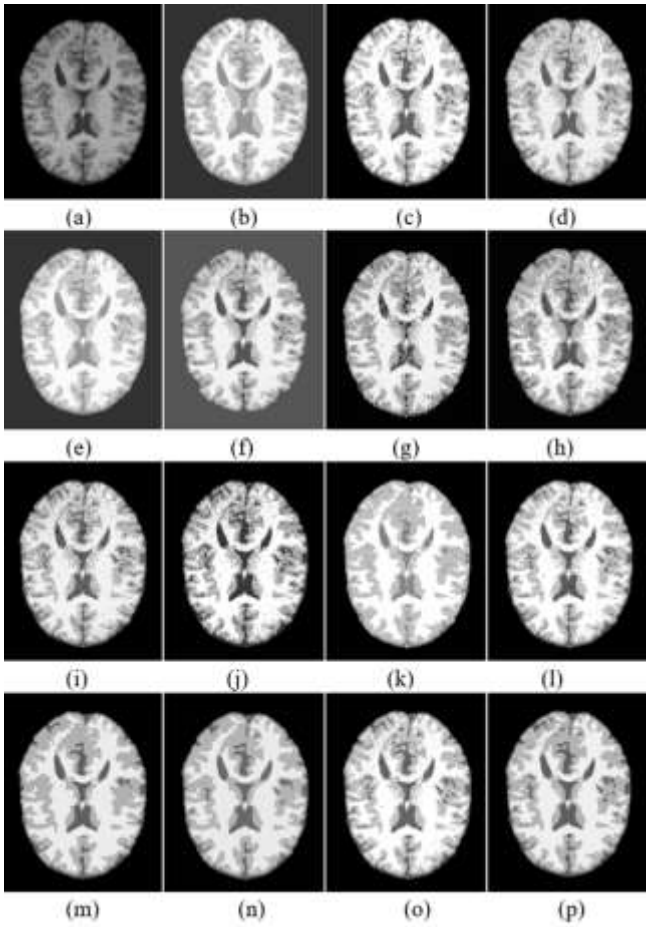

Figure 1. Visual results of different algorithms in the segmentation of a simulated MRI image (Brain Web, slice 86) with 40% INU and 9% noise. (a) Input, (b) Ground truth, (c) MICO, (d) GMM, (e) CSFCM, (f) ARKFCM, (g) FCMPSO, (h) FCMWOA, (i) FCMGWO, (j) AHHO, (k) SFCMEMBC, (l) BCIFCMSNI, (m) FRFCM, (n) RFCM, (o) FBKPCS, and (p) proposed CSGKIT.

4.4. Experimental Results on OASIS Dataset

For further examination, the segmentation performance was repeated for evaluation on T1-weighted MRI images from the OASIS dataset. Figure 3 shows qualitative results for an OASIS image, while Table 5 summarizes the average values of *DS*, *JS*, and *CS* for WM, GM, and CSF. Additionally, Figure 4 presents a boxplot comparing the average *DS* values for WM, GM, and CSF across the algorithms. Key insights from these results are as follows:

(1) Table 5 demonstrates that the proposed CSGKIT algorithm secures the top *DS* values in WM and GM segmentation, *JS* in WM segmentation, and *CS* in WM and GM segmentation.

(2) Population-based approaches, such as FCMPSO and FCMWOA, along with ARKFCM, exhibit the poorest performance. Figure 3(g) shows that FCMPSO often misclassifies the background as WM, while Figure 3(h) highlights FCMWOA's frequent mislabeling of CSF as the background. Although FCMGWO outperforms FCMPSO and FCMWOA, it remains inadequate for CSF segmentation due to the reliance of FCM-based methods on Euclidean distance, which is unsuitable for compact clusters like CSF. Similarly, the AHHO algorithm, while effective for WM and GM segmentation, struggles with CSF. Figures 3(i) and 3(j) illustrate that both FCMGWO and AHHO frequently misclassify CSF as the background.

(3) The OASIS dataset's high INU levels make bias correction-based methods, such as MICO and BCIFCMSNI, highly effective for WM and GM segmentation. However, BCIFCMSNI performs poorly in CSF segmentation. Figure 3(l) shows that while BCIFCMSNI efficiently identifies WM, GM, and CSF pixels, MICO excels in CSF segmentation but falls short in WM segmentation compared to the proposed CSGKIT algorithm. As shown in Table 5, CSFCM is unsuitable for real MRI image segmentation under INU conditions due to the increased computational complexity from incorporating a bias term into the FCM cost function. Despite not relying on bias estimation, the CSGKIT algorithm outperforms its counterparts in brain tissue segmentation.

(4) The FRFCM, RFCM, and FBKPCS algorithms perform well in WM and GM segmentation but struggle with accurate CSF segmentation due to its compact, small clusters. These methods are less suitable for CSF, which plays a critical role in clearing metabolic waste from the brain. As shown in Table 5, the CSGKIT algorithm, by utilizing the Mahalanobis distance instead of the Euclidean distance, proves more effective for clustering compact data like CSF.

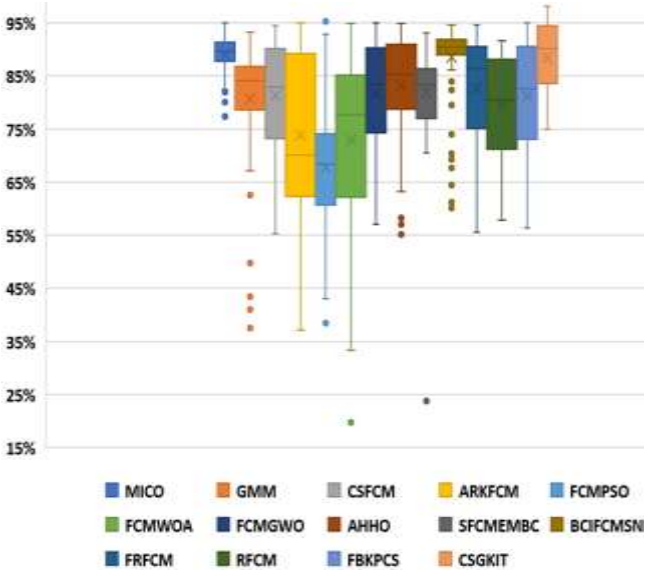

Figure 4. Boxplot comparing the proposed CSGKIT algorithm and other methods in terms of average *DS* criterion for WM, GM, and CSF on the OASIS dataset.

Table 3. Numerical results of all assessed algorithms, including our proposed CSGKIT algorithm, for CSF segmentation on the Brain Web simulated dataset.

Criteria / Methods	*DS* (%) ↑				*JS* (%) ↑				*CS* (%) ↑			
	3% Noise		9% Noise		3% Noise		9% Noise		3% Noise		9% Noise	
	20% INU (μ±S.D)	40% INU (μ±S.D)	20% INU (μ±S.D)	40% INU (μ±S.D)	20% INU (μ±S.D)	40% INU (μ±S.D)	20% INU (μ±S.D)	40% INU (μ±S.D)	20% INU (μ±S.D)	40% INU (μ±S.D)	20% INU (μ±S.D)	40% INU (μ±S.D)
MICO	87.44±0.46	88.44±0.78	82.70±0.46	83.37±4.11	77.89±0.41	79.44±0.49	70.70±0.68	71.67±6.09	97.63±0.19	98.35±0.45	95.13±0.42	95.07±3.61
GMM	89.80±0.54	85.44±0.50	84.52±2.58	84.08±2.48	81.66±0.58	74.92±0.78	73.27±3.64	72.60±3.73	98.69±0.15	97.03±0.17	96.46±1.66	95.85±1.66
CSFCM	83.17±0.41	84.63±0.35	85.08±1.96	84.60±2.18	71.40±0.61	73.51±0.52	74.23±3.02	73.38±3.32	93.13±0.25	94.02±0.22	96.29±1.69	95.31±1.39
ARKFCM	67.08±1.21	64.95±1.26	63.10±0.61	65.98±10.69	56.76±1.50	53.84±1.57	52.12±0.93	53.59±13.16	93.07±1.33	91.24±1.42	90.41±0.59	90.50±11.40
FCMPSO	72.41±3.15	80.39±2.78	65.03±3.06	65.66±12.09	62.27±3.04	71.56±2.75	51.22±2.96	52.37±13.30	92.62±1.03	94.78±1.05	88.33±1.12	88.94±10.14
FCMWOA	75.57±1.47	74.22±1.79	67.34±1.75	68.01±11.98	62.76±1.78	61.36±2.00	52.62±2.96	52.80±13.13	92.46±1.28	91.45±1.77	89.35±4.52	89.80±11.07
FCMGWO	88.65±0.35	89.50±0.69	82.56±2.50	82.18±2.73	80.07±0.56	81.19±0.59	70.38±3.64	69.83±3.92	98.34±0.29	98.21±0.28	95.14±1.20	94.91±1.12
AHHO	89.34±0.42	89.69±0.49	83.17±2.14	82.94±2.13	80.89±0.64	81.76±0.58	71.24±3.17	70.91±3.14	98.77±0.18	98.50±0.48	95.67±1.28	95.56±1.14
SFCMEMBC	60.79±0.58	61.37±5.52	67.56±4.18	68.73±3.97	43.92±0.62	44.50±5.94	51.34±3.27	52.59±4.21	83.07±0.42	82.72±4.07	87.75±4.25	88.27±3.20
BCIFCMSNI	57.04±1.27	47.29±1.06	52.09±0.87	64.26±1.08	49.83±1.31	51.52±0.97	44.07±0.95	58.89±1.94	73.80±1.04	59.06±1.02	74.64±2.62	76.33±1.25
FRFCM	82.52±1.21	83.69±1.09	82.15±1.01	82.13±2.73	70.43±0.95	72.11±0.84	70.10±0.79	70.06±3.27	87.97±0.65	88.54±0.72	88.51±0.93	89.19±2.32
RFCM	83.73±0.77	83.62±0.85	83.80±0.62	83.08±2.89	72.07±0.65	71.92±0.73	76.16±0.48	71.18±3.45	89.00±0.72	89.52±0.68	89.98±0.88	91.02±2.55
FBKPCS	88.84±0.44	89.41±2.89	85.14±1.98	85.15±2.21	80.09±0.55	81.14±3.04	74.95±3.08	74.20±3.38	98.21±0.22	98.03±0.91	96.72±0.96	96.48±0.71
CSGKIT	**91.87±1.13**	**91.19±1.26**	**89.29±1.57**	**88.68±1.75**	**85.06±1.26**	**83.96±1.41**	**80.69±2.40**	**79.76±2.67**	**99.27±0.47**	**99.13±0.88**	**98.60±0.44**	**98.30±0.30**

Table 4. Average execution times of various algorithms on the Brain Web dataset with 40% INU and 9% noise. All values are presented in seconds.

MICO	GMM	CSFCM	ARKFCM	FCMPSO	FCMWOA	FCMGWO	AHHO	SFCMEMBC	BCIFCMSNI	FRFCM	RFCM	FBKPCS	**CSGKIT**
4.17	1.20	0.76	1.87	4.15	3.05	6.50	19.40	0.61	2.85	**0.05**	0.62	0.39	**0.34**

(5) Figure 4 helps discern that the proposed CSGKIT algorithm attains higher segmentation accuracy for brain tissues compared to other methods. Notably, CSGKIT exhibits the lowest standard deviation, indicating consistent performance across WM, GM, and CSF segmentation. As shown in Figure 3, all algorithms, except CSGKIT, frequently mislabel CSF pixels, leading to suboptimal segmentation. In contrast, CSGKIT effectively and accurately segments CSF tissue, demonstrating its robustness.

(6) The quantitative evaluation presented in Tables 5 and 6 clearly demonstrates the superior performance of the proposed algorithm compared to a wide range of benchmark segmentation methods. In terms of the *DS*, *JS*, and *CS* criteria, proposed algorithm consistently achieved the highest mean values across all brain tissues (WM, GM, and CSF), with relatively low standard deviations ($\mu \pm S.D.$), reflecting its robustness and stability in handling structural and intensity variations in MRI data. Specifically, CSGKIT obtained *DS* values of 95.87%, 87.43%, and 83.42% for WM, GM, and CSF, respectively, and maintained superior performance in *JS* (91.31%, 76.83%, 73.70%) and *CS* (98.02%, 96.64%, 91.22%) criteria, outperforming all competing methods by a statistically significant margin. To verify the reliability of these improvements, a two-sample t-test was performed between the results of the proposed algorithm and each competing method under all evaluation criteria. The resulting p-values (ρ) are provided in Table 6. As shown, most p-values are below the 0.05 threshold, indicating that the observed improvements are statistically significant at the 95% confidence level. Only a few isolated cases (such as the WM region under *DS* criterion versus FCMGWO and FBKPCS) exhibited p-values above 0.05, suggesting that the differences in those specific cases were not statistically significant. Nonetheless, the overall statistical evidence strongly supports the superior segmentation accuracy and consistency of the proposed method. These findings confirm that the CSGKIT algorithm not only achieves higher segmentation precision but also demonstrates statistically validated improvements through rigorous t-test analysis. The

combination of adaptive information-theoretic measures and conditional spatial information contributes to its ability to minimize boundary ambiguity and enhance tissue differentiation, leading to more accurate and stable MRI brain segmentation results.

(7) Table 7 presents the average running times for various algorithms. The results indicate that FCMPSO, FCMWOA, FCMGWO, and AHHO algorithms are computationally expensive. Similarly, contour-based methods like MICO have longer execution times. In contrast, the FRFCM and CSGKIT algorithms demonstrate the lowest execution times, highlighting their efficiency compared to other approaches.

Table 5. Numerical results of all assessed algorithms, including our proposed CSGKIT algorithm, for segmentation task on the OASIS dataset.

Criteria / Methods	*DS* (%) ↑			*JS* (%) ↑			*CS* (%) ↑		
	WM (μ±S.D)	GM (μ±S.D)	CSF (μ±S.D)	WM (μ±S.D)	GM (μ±S.D)	CSF (μ±S.D)	WM (μ±S.D)	GM (μ±S.D)	CSF (μ±S.D)
MICO	91.79±0.25	86.03±0.52	**88.54±0.70**	84.92±0.42	75.82±0.75	**80.06±1.02**	94.55±0.27	95.43±0.19	**94.83±0.55**
GMM	90.14±0.40	77.61±1.73	75.21±1.36	82.26±0.62	65.74±1.69	62.03±1.63	93.09±0.33	90.42±1.08	82.67±1.56
CSFCM	94.09±0.12	80.62±1.13	69.56±1.94	88.85±0.21	68.91±1.48	56.66±2.27	97.01±0.19	94.12±0.45	85.62±1.26
ARKFCM	93.15±0.72	70.50±1.85	57.21±2.67	87.66±0.77	57.44±2.19	44.87±2.71	95.48±0.74	92.09±0.66	77.83±1.71
FCMPSO	80.17±2.29	67.26±2.35	53.98±2.51	72.06±2.72	55.05±2.51	41.17±2.49	89.59±1.13	91.57±0.69	80.84±1.36
FCMWOA	86.84±1.18	71.56±2.21	60.71±2.26	78.27±1.50	59.63±2.31	47.12±2.22	86.35±1.83	91.85±0.78	83.00±1.91
FCMGWO	95.12±0.12	82.19±1.03	68.56±1.87	90.61±0.21	70.98±1.39	55.20±2.16	97.01±0.12	95.14±0.36	84.44±1.09
AHHO	95.08±0.13	83.44±1.00	71.36±1.85	90.32±0.24	72.70±1.32	58.53±2.16	97.26±0.12	95.62±0.34	85.94±1.09
SFCMEMBC	93.94±0.25	82.82±0.92	68.73±1.18	88.66±0.37	71.57±1.17	53.51±1.31	97.16±0.56	92.09±0.59	81.46±1.71
BCIFCMSNI	93.35±0.23	87.10±0.61	83.73±1.59	87.61±0.39	**78.39±0.85**	74.37±1.75	96.66±0.19	96.04±0.23	93.44±0.94
FRFCM	93.95±0.12	78.17±1.12	66.53±1.91	88.61±0.20	65.11±1.46	52.77±2.22	95.60±0.19	93.89±0.42	83.67±1.27
RFCM	94.42±0.14	82.26±0.94	71.83±1.85	89.46±0.24	71.24±1.23	59.31±2.13	96.60±0.20	94.57±0.40	86.47±1.21
FBKPCS	95.06±0.12	81.18±1.11	67.78±1.93	90.47±0.22	69.72±1.50	54.47±2.23	97.11±0.13	95.08±0.39	83.91±1.15
CSGKIT	**95.87±0.12**	**87.43±0.62**	83.42±1.33	**91.31±0.19**	76.83±1.07	73.70±1.53	**98.02±0.15**	**96.64±0.21**	91.22±1.01

Table 6. Statistical significance (*p*-values) of segmentation performance differences between the proposed CSGKIT algorithm and competing methods across *DS*, *JS*, and *CS* criteria for WM, GM, and CSF tissues on OASIS dataset.

Criteria / Methods	*DS* Criterion			*JS* Criterion			*CS* Criterion		
	WM	GM	CSF	WM	GM	CSF	WM	GM	CSF
MICO	1.10e-43	0.9965	1.44e-12	4.17e-46	0.6142	3.30e-11	7.71e-30	0.1584	1.25e-12
GMM	6.30e-45	3.76e-10	6.92e-09	9.54e-50	7.04e-13	6.97e-11	2.08e-45	5.28e-12	3.37e-09
CSFCM	5.63e-53	1.03e-29	1.12e-54	5.68e-54	4.20e-33	2.16e-58	1.86e-07	4.08e-35	8.65e-33
ARKFCM	3.27e-05	1.48e-49	1.84e-56	8.48e-10	1.02e-42	1.73e-65	4.73e-05	2.46e-30	3.88e-44
FCMPSO	2.90e-17	5.93e-24	5.07e-37	9.47e-19	4.87e-25	2.21e-38	7.38e-20	2.82e-20	1.56e-22
FCMWOA	2.28e-19	1.88e-15	5.75e-26	1.31e-24	1.39e-16	2.15e-28	3.58e-15	5.73e-13	1.91e-06
FCMGWO	0.0655	1.17e-21	1.38e-60	0.0681	7.30e-23	5.33e-63	4.88e-05	3.01e-17	1.07e-45
AHHO	0.1812	1.05e-26	3.35e-57	0.2153	1.62e-27	2.46e-60	0.0051	2.38e-19	4.82e-43
SFCMEMBC	2.88e-10	0.0016	1.28e-15	1.11e-12	8.86e-04	3.81e-18	0.5018	7.72e-12	1.19e-06
BCIFCMSNI	3.23e-18	0.0400	0.3250	4.71e-19	0.0571	0.2939	7.77e-06	0.0583	1.81e-04
FRFCM	4.99e-20	3.60e-14	1.74e-40	1.22e-20	4.30e-16	2.10e-44	2.56e-16	3.36e-22	3.56e-18
RFCM	5.28e-32	2.01e-53	1.18e-59	5.57e-33	7.42e-59	1.39e-62	8.85e-43	5.35e-44	6.24e-47
FBKPCS	0.1188	1.23e-24	4.70e-60	0.1170	1.02e-25	3.50e-63	0.0038	1.90e-17	6.46e-50

Table 7. Average execution times of various algorithms on the OASIS dataset. All values are presented in seconds.

MICO	GMM	CSFCM	ARKFCM	FCMPSO	FCMWOA	FCMGWO	AHHO	SFCMEMBC	BCIFCMSNI	FRFCM	RFCM	FBKPCS	**CSGKIT**
3.72	1.33	0.56	1.82	7.95	3.41	6.57	20.38	1.05	3.18	**0.11**	1.16	0.59	**0.39**

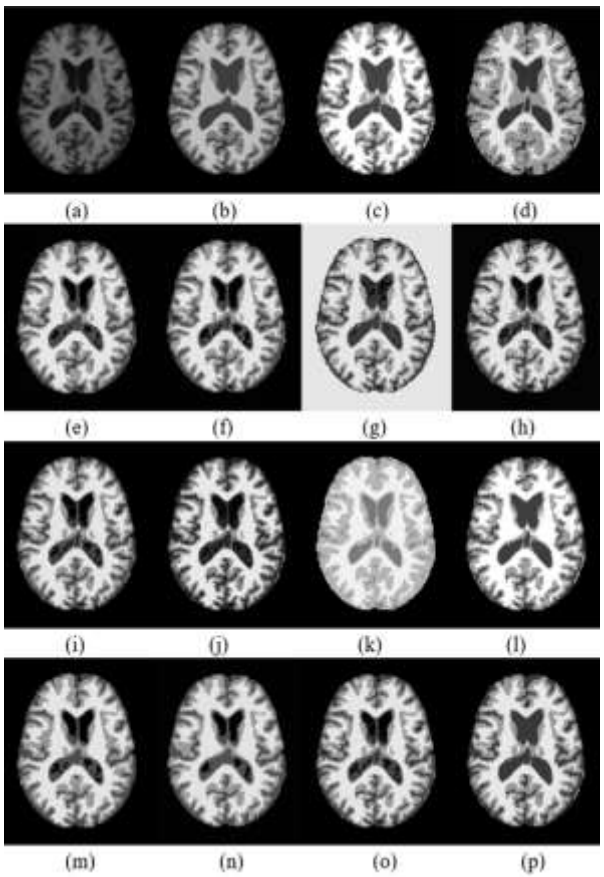

Figure 3. Visual results of different algorithms in the segmentation of a sample from the OASIS dataset. (a) Input, (b) Ground truth, (c) MICO, (d) GMM, (e) CSFCM, (f) ARKFCM, (g) FCMPSO, (h) FCMWOA, (i) FCMGWO, (j) AHHO, (k) SFCMEMBC, (l) BCIFCMSNI, (m) FRFCM, (n) RFCM, (o) FBKPCS, and (p) proposed CSGKIT.

5. Conclusion and Future Work

Traditional FCM-based approaches rely on Euclidean distance for clustering, which fails to account for variations in distances within compact and similarly shaped clusters. This limitation is particularly problematic for CSF, a compact cluster critical for clearing metabolic waste from the brain. The reliance on Euclidean distance often leads to misclassification of CSF into other classes. Additionally, noise and INU negatively impact clustering performance. To address these challenges, this study proposed the CSGKIT algorithm for tissue segmentation in T1-weighted MRI images. Unlike conventional approaches, CSGKIT does not require computing distances among pixels within local spatial neighborhoods. Our algorithm introduces three key innovations: (i) information theory enhances robustness to noise and improves segmentation accuracy; (ii) Mahalanobis distance replaces Euclidean distance, providing better handling of compact and irregular clusters like CSF; and (iii) a conditional spatial approach incorporates local spatial relationships through a fuzzy weighted membership matrix. The proposed algorithm is computationally efficient, does not require complex parameter tuning, and achieves high segmentation accuracy. Experimental evaluations on the BrainWeb simulated and OASIS datasets demonstrated that the CSGKIT algorithm outperforms peer methods in robustness to noise and INU. Additionally, it maintains consistent performance across all image slices and effectively preserves edges under varying conditions. While the CSGKIT algorithm shows promising results, it does not fully leverage the neighboring information of each pixel, which could further enhance segmentation accuracy. Future work may explore integrating neighboring information more effectively to improve segmentation outcomes. Furthermore, developing an adaptive mechanism within the Gustafson-Kessel framework to automatically select the number of clusters could be a potential direction for improvement. Lastly, incorporating bias field correction into the CSGKIT cost function may further enhance its robustness. Additionally, although this study focuses on T1-weighted MRI images as the standard protocol for structural brain imaging, future research should investigate extending CSGKIT to other MRI modalities such as T2-weighted and FLAIR images, which may require modality-specific parameter optimization to account for different tissue contrast characteristics.

References

[1] S. Kollem, C. R. Prasad, J. Ajayan, V. Malathy and A. Subbarao, "Brain tumor MRI image segmentation using an optimized multi-kernel FCM method with a pre-processing stage," Multimedia Tools and Applications, vol. 82, no. 14, pp. 20741–20770, 2023.

[2] S. Alagarsamy, V. Govindaraj and A. Senthilkumar, "Automated brain tumor segmentation for MR brain images using artificial bee colony combined with interval type-II fuzzy technique," IEEE Transactions on Industrial Informatics, vol. 19, no. 11, pp. 11150–11159, 2023.

[3] C. Singh, S. K. Ranade, D. Kaur and A. Bala, "An Intuitionistic Fuzzy C-Means and Local Information-Based DCT Filtering for Fast Brain MRI Segmentation," Journal of Imaging Informatics in Medicine, vol. 1, no. 1, pp. 1–24, 2024.

[4] J. Lyu, X. Chen, S. A. AlQahtani and M. S. Hossain, "Multi-modality MRI fusion with patch complementary pre-training for internet of medical things-based smart healthcare," Information Fusion, vol. 107, pp. 102342, 2024.

[5] N. Aboubakr, M. Popova and J. L. Crowley, "Color-based fusion of MRI modalities for brain tumor segmentation," in Proc. Int. Conf. on Medical Imaging and Computer-Aided Diagnosis (MICAD), pp. 89–97, 2021.

[6] A. Alijamaat, A. R. NikravanShalmani and P. Bayat, "Diagnosis of Multiple Sclerosis Disease in Brain MRI Images using Convolutional Neural Networks based on Wavelet Pooling," Journal of AI and Data Mining, vol. 9, no. 2, pp. 161-168, 2021.

[7] M. Hassan, I. Murtza, A. Hira, S. Ali and S. K. Kifayat, "Robust spatial fuzzy GMM based MRI segmentation and carotid artery plaque detection in ultrasound images," Computer Methods and Programs in Biomedicine, vol. 175, pp. 179–192, 2019.

[8] S. Natarajan, V. Govindaraj, Y. Zhang, P. R. Murugan, K. Balasubramanian, K. Kandasamy and K. Ejaz, "Minimally parametrized segmentation framework with dual metaheuristic optimisation algorithms and FCM for detection of anomalies in MR brain images," Biomedical Signal Processing and Control, vol. 78, pp. 103866, 2022.

[9] I. Khatri, D. Kumar and A. Gupta, "A noise robust kernel fuzzy clustering based on picture fuzzy sets and KL divergence measure for MRI image segmentation," Applied Intelligence, vol. 53, no. 13, pp. 16487–16518, 2023.

[10] E. H. Houssein, N. Abdalkarim, K. Hussain and E. Mohamed, "Accurate multilevel thresholding image segmentation via oppositional Snake Optimization algorithm: Real cases with liver disease," Computers in Biology and Medicine, vol. 169, pp. 107922, 2024.

[11] M. B. Bawil, M. Shamsi, A. S. Bavil and S. Danishvar, "Specialized gray matter segmentation via a generative adversarial network: application on brain white matter hyperintensities classification," Frontiers in Neuroscience, vol. 18, pp. 1–10, 2024.

[12] E. H. Houssein, M. M. Emam and A. A. Ali, "An efficient multilevel thresholding segmentation method for thermography breast cancer imaging based on improved chimp optimization algorithm," Expert Systems with Applications, vol. 185, pp. 115651, 2021.

[13] G. Ma and X. Yue, "An improved whale optimization algorithm based on multilevel threshold image segmentation using the Otsu method," Engineering Applications of Artificial Intelligence, vol. 113, pp. 104960, 2022.

[14] T. Lang and T. Sauer, "Feature-Adaptive Interactive Thresholding of Large 3D Volumes," arXiv preprint, arXiv:2210.06961, 2022.

[15] B. Dong, G. Weng, Q. Bu, Z. Zhu and J. Ni, "An active contour model based on shadow image and reflection edge for image segmentation," Expert Systems with Applications, vol. 238, pp. 122330, 2024.

[16] Y. Chen, L. Wu, G. Wang, H. He, G. Weng and H. Chen, "An active contour model for image segmentation using morphology and nonlinear Poisson's equation," Optik, vol. 287, pp. 170997, 2023.

[17] H. Zia, A. Niaz and K. N. Choi, "Active Contour Model for Image Segmentation," in Proc. Asia Conf. on Advanced Robotics, Automation, and Control Engineering (ARACE), pp. 1–6, 2022.

[18] C. Li, J. C. Gore and C. Davatzikos, "Multiplicative intrinsic component optimization (MICO) for MRI bias field estimation and tissue segmentation," Magnetic Resonance Imaging, vol. 32, no. 7, pp. 913–923, 2014.

[19] P. D. Dunning and H. A. Kim, "Introducing the sequential linear programming level-set method for topology optimization," Structural and Multidisciplinary Optimization, vol. 51, no. 3, pp. 631–643, 2015.

[20] S. K. Adhikari, J. K. Sing, D. K. Basu and M. Nasipuri, "Conditional spatial fuzzy C-means clustering algorithm for segmentation of MRI images," Applied Soft Computing, vol. 34, pp. 758–769, 2015

[21] A. Elazab, C. Wang, F. Jia, J. Wu, G. Li and Q. Hu, "Segmentation of brain tissues from magnetic resonance images using adaptively regularized kernel-based fuzzy C-means clustering," Computational and Mathematical Methods in Medicine, vol. 2015, no. 1, pp. 485495, 2015.

[22] J. Song and Z. Zhang, "A modified robust FCM model with spatial constraints for brain MR image segmentation," Information, vol. 10, no. 2, pp. 74, 2019.

[23] J. Qiao, X. Cai, Q. Xiao, Z. Chen, P. Kulkarni, C. Ferris and S. Sridhar, "Data on MRI brain lesion segmentation using K-means and Gaussian Mixture Model-Expectation Maximization," Data in Brief, vol. 27, pp. 104628, 2019.

[24] R. Meena Prakash, R. Shantha and S. Kumari, "Spatial fuzzy C-means and expectation maximization algorithms with bias correction for segmentation of MR brain images," Journal of Medical Systems, vol. 41, no. 9, pp. 1–9, 2017.

[25] M. Singh, A. Verma and N. Sharma, "Multi-objective noise estimator for the applications of de-noising and segmentation of MRI data," Biomedical Signal Processing and Control, vol. 46, pp. 249–259, 2018.

[26] P. Ghosh, K. Mali and S. K. Das, "Chaotic firefly algorithm-based fuzzy C-means algorithm for segmentation of brain tissues in magnetic resonance images," Journal of Visual Communication and Image Representation, vol. 54, pp. 63–79, 2018.

[27] A. F. Jafargholkhanloo and M. Shamsi, "Cephalometry analysis of facial soft tissue based on two orthogonal views applicable for facial plastic surgeries," Multimedia Tools and Applications, vol. 82, no. 20, pp. 30643–30668, 2023.

[28] H. Verma, D. Verma and P. K. Tiwari, "A population based hybrid FCM-PSO algorithm for

clustering analysis and segmentation of brain image," Expert Systems with Applications, vol. 167, pp. 114121, 2021.

[29] S. Tongbram, B. A. Shimray, L. S. Singh and N. Dhanachandra, "A novel image segmentation approach using FCM and whale optimization algorithm," Journal of Ambient Intelligence and Humanized Computing, vol. 12, no. 8, pp. 1–15, 2021.

[30] R. Bandyopadhyay, R. Kundu, D. Oliva and R. Sarkar, "Segmentation of brain MRI using an altruistic Harris Hawks' Optimization algorithm," Knowledge-Based Systems, vol. 232, pp. 107468, 2021.

[31] A. Kouhi, H. Seyedarabi and A. Aghagolzadeh, "Robust FCM clustering algorithm with combined spatial constraint and membership matrix local information for brain MRI segmentation," Expert Systems with Applications, vol. 146, pp. 113159, 2020.

[32] M. Tavakoli-Zaniani, Z. Sedighi-Maman and M. H. F. Zarandi, "Segmentation of white matter, grey matter and cerebrospinal fluid from brain MR images using a modified FCM based on double estimation," Biomedical Signal Processing and Control, vol. 68, pp. 102615, 2021.

[33] D. Kumar, I. Khatri, A. Gupta and R. Gusain, "Kernel picture fuzzy clustering with spatial neighborhood information for MRI image segmentation," Soft Computing, vol. 26, no. 22, pp. 12717–12740, 2022.

[34] S. Vinurajkumar and S. Anandhavelu, "An Enhanced Fuzzy Segmentation Framework for extracting white matter from T1-weighted MR images," Biomedical Signal Processing and Control, vol. 71, pp. 103093, 2022.

[35] D. Kumar, R. K. Agrawal and P. Kumar, "Bias-corrected intuitionistic fuzzy c-means with spatial neighborhood information approach for human brain MRI image segmentation," IEEE Transactions on Fuzzy Systems, vol. 30, no. 3, pp. 687–700, 2020.

[36] R. Solanki and D. Kumar, "Probabilistic intuitionistic fuzzy c-means algorithm with spatial constraint for human brain MRI segmentation," Multimedia Tools and Applications, vol. 82, no. 22, pp. 33663–33692, 2023.

[37] P. Kumar, R. K. Agrawal and D. Kumar, "Fast and robust spatial fuzzy bounded k-plane clustering method for human brain MRI image segmentation," Applied Soft Computing, vol. 133, pp. 109939, 2023.

[38] S. Mohammadi, S. Ghaderi, K. Ghaderi, M. Mohammadi and M. H. Pourasl, "Automated segmentation of meningioma from contrast-enhanced T1-weighted MRI images in a case series using a marker-controlled watershed segmentation and fuzzy C-means clustering machine learning algorithm," International Journal of Surgery Case Reports, vol. 111, pp. 108818, 2023.

[39] C. Singh, S. K. Ranade, D. Kaur and A. Bala, "A novel approach for brain MRI segmentation and image restoration under intensity inhomogeneity and noisy conditions," Biomedical Signal Processing and Control, vol. 87, pp. 105348, 2024.

[40] B. Jafrasteh, M. Lubián-Gutiérrez, S. P. Lubián-López and I. Benavente-Fernández, "Enhanced Spatial Fuzzy C-Means Algorithm for Brain Tissue Segmentation in T1 Images," Neuroinformatics, vol. 2024, no. 1, pp. 1–14, 2024.

[41] J. C. Bezdek, R. Ehrlich, and W. Full, "FCM: The fuzzy c-means clustering algorithm," Computers & Geosciences, vol. 10, no. 2–3, pp. 191–203, 1984.

[42] L. Szilagyi, Z. Benyo, S. M. Szilágyi and H. S. Adam, "MR brain image segmentation using an enhanced fuzzy c-means algorithm," in Proc. 25th Annu. Int. Conf. IEEE Engineering in Medicine and Biology Society, vol. 1, pp. 724–726, 2003.

[43] W. Cai, S. Chen and D. Zhang, "Fast and robust fuzzy c-means clustering algorithms incorporating local information for image segmentation," Pattern Recognition, vol. 40, no. 3, pp. 825–838, 2007.

[44] S. Krinidis and V. Chatzis, "A robust fuzzy local information C-means clustering algorithm," IEEE Transactions on Image Processing, vol. 19, no. 5, pp. 1328–1337, 2010.

[45] M. Gong, Y. Liang, J. Shi, W. Ma and J. Ma, "Fuzzy c-means clustering with local information and kernel metric for image segmentation," IEEE Transactions on Image Processing, vol. 22, no. 2, pp. 573–584, 2012.

[46] T. Lei, X. Jia, Y. Zhang, L. He, H. Meng and A. K. Nandi, "A significantly fast and robust fuzzy c-means clustering algorithm based on morphological reconstruction and membership filtering," IEEE Transactions on Fuzzy Systems, vol. 26, no. 5, pp. 3027–3041, 2018.

[47] C. Wang, W. Pedrycz, Z. Li and M. Zhou, "Residual-driven fuzzy C-means clustering for image segmentation," IEEE/CAA Journal of Automatica Sinica, vol. 8, no. 4, pp. 876–889, 2020.

[48] R. Krishnapuram and J. Kim, "A note on the Gustafson–Kessel and adaptive fuzzy clustering algorithms," IEEE Transactions on Fuzzy Systems, vol. 7, no. 4, pp. 453–461, 1999.

[49] D. Dovžan and I. Škrjanc, "Recursive clustering based on a Gustafson–Kessel algorithm," Evolving Systems, vol. 2, no. 1, pp. 15–24, 2011.

[50] R. Babuka, P. J. Van der Veen and U. Kaymak, "Improved covariance estimation for Gustafson–Kessel clustering," in Proc. 2002 IEEE World Congress on Computational Intelligence, vol. 2, pp. 1081–1085, 2002.

[51] D. E. Gustafson and W. C. Kessel, "Fuzzy clustering with a fuzzy covariance matrix," in Proc. 1978 IEEE Conf. Decision and Control including the

17th Symposium on Adaptive Processes, pp. 761–766, 1979.

[52] Z. Wang, Q. Song, Y. C. Soh and K. Sim, "An adaptive spatial information-theoretic fuzzy clustering algorithm for image segmentation," Computer Vision and Image Understanding, vol. 117, no. 10, pp. 1412–1420, 2013.

[53] A. F. Jafargholkhanloo and M. Shamsi, "Quantitative analysis of facial soft tissue using weighted cascade regression model applicable for facial plastic surgery," Signal Processing: Image Communication, vol. 121, pp. 117086, 2024.

[54] BrainWeb [online], available: https://brainweb.bic.mni.mcgill.ca/cgi/brainweb1

[55] D. S. Marcus, T. H. Wang, J. Parker, J. G. Csernansky, J. C. Morris and R. L. Buckner, "Open Access Series of Imaging Studies (OASIS): Cross-sectional MRI data in young, middle aged, nondemented, and demented older adults," Journal of Cognitive Neuroscience, vol. 19, no. 9, pp. 1498–1507, 2007.

بخش‌بندی تصاویر MRI مغز با استفاده از الگوریتم گستافسون-کسل مکانی شرطی براساس تئوری اطلاعات

علی فهمی جعفرقلخانلو[1*]، موسی شمسی[2] و مهدی بشیری باویل[2]

[1] گروه علوم مهندسی، دانشکده فناوری‌های نوین، دانشگاه محقق اردبیلی، نمین، ایران.

[2] گروه بیوالکتریک، دانشکده مهندسی پزشکی، دانشگاه صنعتی سهند، تبریز، ایران.

ارسال ۲۰۲۵/۰۸/۲۰؛ بازنگری ۲۰۲۵/۱۰/۲۴؛ پذیرش ۲۰۲۵/۱۱/۳۰

چکیده:

تصویربرداری تشدید مغناطیسی (MRI) معمولاً با نویز و ناهمگنی شدت (INU) همراه بوده و فرآیند بخش‌بندی بافت‌های مغزی را با چالش‌های جدی مواجه می‌کند. الگوریتم خوشه‌بندی فازی C-میانگین (FCM)، که یکی از روش‌های پرکاربرد در بخش‌بندی تصاویر پزشکی بوده که نسبت به نویز بسیار بوده و نرخ همگرایی آن به توزیع داده‌ها وابسته است. این الگوریتم از معیار فاصله اقلیدسی استفاده می‌کند که توانایی انطباق با تغییرات توزیع نقاط داده در خوشه‌های فشرده و با شکل‌های مشابه را ندارد و همچنین از نظر محلی با شکل‌های متفاوت خوشه‌ها سازگار نیست. در این مقاله، یک الگوریتم خوشه‌بندی شرطی مکانی گستافسون–کسل مبتنی بر تئوری اطلاعات (CSGKIT) به‌منظور غلبه بر این محدودیت‌ها ارائه می‌شود. در گام نخست، از تئوری اطلاعات برای افزایش مقاومت الگوریتم در برابر نویز و بهبود دقت بخش‌بندی استفاده شده است. در گام بعدی، فاصله ماهالانوبیس به‌عنوان معیار شباهت به‌کار گرفته می‌شود که نسبت به فاصله اقلیدسی، قابلیت بیشتری در تطبیق با شکل‌ها و پراکندگی‌های ناهمسان خوشه‌ها دارد. در نهایت، یک رویکرد مکانی شرطی با به‌کارگیری ماتریس عضویت وزن‌دهی‌شده فازی، تعاملات مکانی محلی میان پیکسل‌های مجاور را در مدل لحاظ می‌کند. الگوریتم پیشنهادی CSGKIT بر روی دو پایگاه داده، شامل داده شبیه‌سازی‌شده BrainWeb و مجموعه داده OASIS، مورد ارزیابی قرار گرفته است. نتایج تجربی نشان می‌دهد که الگوریتم CSGKIT در مقایسه با سایر الگوریتم‌های مبتنی بر FCM، از دقت بالاتری در بخش‌بندی انواع مختلف بافت‌ها برخوردار است.

کلمات کلیدی: بخش‌بندی بافت‌های مغزی، گستافسون-کسل مکانی شرطی، بخش‌بندی تصویر، تئوری اطلاعات.